

The nonlinear instability in the Large Plasma Device

B. Friedman,^{1, a)} T.A. Carter,¹ M.V. Umansky,² D. Schaffner,¹ and I. Joseph²

¹⁾*Department of Physics and Astronomy, University of California, Los Angeles, California 90095-1547, USA*

²⁾*Lawrence Livermore National Laboratory, Livermore, California 94550, USA*

Simulations of drift wave turbulence in the Large Plasma Device (LAPD) [W. Gekelman *et al.*, Rev. Sci. Inst. **62**, 2875 (1991)] reveal that a nonlinear instability primarily drives the turbulence despite the presence of a linear drift wave instability. A prior paper by the authors [B. Friedman *et al.*, Phys Plasmas **19**, 102307 (2012)] used an energy dynamics analysis to show that the nonlinear instability preferentially drives $k_{\parallel} = 0$ potential energy fluctuations. These fluctuations then three-wave couple to $k_{\parallel} \neq 0$ potential energy fluctuations in order to access the adiabatic response to transfer their energy to kinetic energy fluctuations. The simulation in that paper, however, enforced periodic axial boundary conditions. This paper extends that work by applying axial sheath boundary conditions to the same model and comparing this new simulation with the old periodic one. It also looks more in depth at the consequences of the nonlinear instability, such as the affect on the turbulent structure and on the quasilinear flux. The main finding is that the linear physics changes significantly when sheath boundaries are used due to the presence of a strongly unstable conducting wall mode. The turbulent state, however, is barely affected by the sheath boundaries as the nonlinear instability remains robust to the changed linear physics.

^{a)}Electronic mail: friedman@physics.ucla.edu

I. INTRODUCTION

In the past, several studies of simulations of magnetized plasma turbulence that used different plasma models and/or scenarios uncovered that nonlinear instabilities drove the turbulence. Sometimes the instabilities were found to be of the subcritical¹⁻⁶ or supercritical^{7,8} variety, while at other times the nonlinear instability simply overpowered a particular linear instability to drive the turbulence⁹⁻¹⁷. In the scenario applicable to turbulence in the Large Plasma Device (LAPD)¹⁸ – in which the magnetic fields lines are straight and without shear – several studies showed the turbulence to be driven by a nonlinear instability of this last type, where the nonlinear instability imposed itself over a linear drift-wave instability^{9,10,13,17}. One of these¹⁷ used LAPD experimental parameters and profiles in the simulation and demonstrated that the nonlinear instability was necessary to drive turbulence with characteristics similar to that of the experiment. Now, these studies^{9,10,13,17} all ascertained that the mechanism driving the nonlinear instability relies upon axial wavenumber transfers between $k_{\parallel} = 0$ and $k_{\parallel} \neq 0$ structures. The reason is that the turbulence self-organizes to preferentially drive $k_{\parallel} = 0$ density and temperature fluctuations, taking energy from the density and temperature equilibrium gradients. But in order to access the adiabatic response, which transfers energy into the dynamically critical $E \times B$ flows, the $k_{\parallel} = 0$ fluctuations must transfer their energy through nonlinear three-wave decay into $k_{\parallel} \neq 0$ fluctuations.

All of these straight magnetic field simulations, however, employed periodic boundary conditions in the axial (z) direction. Now, not only are periodic boundary conditions unphysical, but they can also prevent the linear drift waves from accessing their most unstable axial structures. In other words, the largest scale axial fluctuations that can fit in the machine when periodic boundaries are imposed are those with a single wavelength. Half-wavelength or quarter-wavelength fluctuations are not allowed even though they have larger linear growth rates in the LAPD configuration. Furthermore, it is well known that wall properties can drive linear instabilities like in the case of resistive wall modes or conducting wall modes¹⁹, with the latter being relevant to the LAPD configuration. Clearly, periodic boundary simulations miss all of this wall physics. Axial boundary conditions, therefore, have a significant affect on the linear stability properties of the system, which is shown in detail in Section III. And since the nonlinear instability relies upon axial wavelength dy-

namics to work, it is reasonable to speculate that the boundaries also might have a significant affect on the nonlinear instability properties.

The real axial boundaries in LAPD are complicated. One side of the device contains an emitting cathode behind a mesh annode, and in front of that sits a biased limiter with radius slightly less than the cathode radius²⁰. The other side contains a floating mesh plate, which is likely shielded by a layer of neutral gas. Not only is it difficult to determine what the actual axial boundary conditions are, it is also difficult to develop and implement models for the boundaries. Thus, this paper explores the idealized situation in which both axial ends of the machine are perfectly conducting metal plates, which can be modeled with a Bohm sheath condition. The main finding is that while the linear stability properties of this sheath boundary simulation are significantly different from the simulation with periodic boundaries, the nonlinear instability still dominates the turbulent drive. Therefore, the qualitative properties of the turbulence and the turbulent dynamics are similar between the two simulations. Quantitatively, however, there are some differences between the simulations including the nonlinear instability being somewhat less dominant and the dissipation stronger in the simulation with sheath boundaries.

The paper is organized as follows: Section II presents the model used in the simulations, while Sec. III goes over the origins and properties of the linear instabilities in the model. Then Sec. IV develops the energetics equations that are used in Sec. V to reveal the details of the nonlinear instability in both the simulation with periodic axial boundary conditions and the one with sheath axial boundary conditions. Next, Sec. VI looks at some properties of the turbulence, such as its mode structure and flux profile, which are greatly affected by the nonlinear instability, and finally, conclusions are made in Sec. VII.

II. THE DRIFT WAVE MODEL

A Braginskii-based fluid model²¹ is used to simulate global drift wave turbulence in LAPD using the BOUT++ code²². The evolved variables in the model are the plasma density, N , the electron fluid parallel velocity $v_{\parallel e}$, the potential vorticity $\varpi \equiv \nabla_{\perp} \cdot (N_0 \nabla_{\perp} \phi)$, and the electron temperature T_e . The ions are assumed cold in the model ($T_i = 0$), and sound wave effects are neglected ($v_i = 0$). Details of the simulation code, derivations of the model, grid convergence studies, and analyses of simplified models may be found in previous LAPD

simulation studies^{17,23–26}.

The equations are developed with Bohm normalizations: lengths are normalized to the ion sound gyroradius, times to the ion cyclotron time, velocities to the sound speed, densities to the equilibrium peak density, and electron temperatures and potentials to the equilibrium peak electron temperature. These normalizations are constants (not functions of radius) and are calculated from these reference values: the magnetic field is 1 kG, the ion unit mass is 4, the peak density is $2.86 \times 10^{12} \text{ cm}^{-3}$, and the peak electron temperature is 6 eV. The equations are:

$$\partial_t N = -\mathbf{v}_E \cdot \nabla N_0 - N_0 \nabla_{\parallel} v_{\parallel e} + \mu_N \nabla_{\perp}^2 N + S_N + \{\phi, N\}, \quad (1)$$

$$\partial_t v_{\parallel e} = -\frac{m_i}{m_e} \frac{T_{e0}}{N_0} \nabla_{\parallel} N - 1.71 \frac{m_i}{m_e} \nabla_{\parallel} T_e + \frac{m_i}{m_e} \nabla_{\parallel} \phi - \nu_e v_{\parallel e} + \{\phi, v_{\parallel e}\}, \quad (2)$$

$$\partial_t \varpi = -N_0 \nabla_{\parallel} v_{\parallel e} - \nu_{in} \varpi + \mu_{\phi} \nabla_{\perp}^2 \varpi + \{\phi, \varpi\}, \quad (3)$$

$$\begin{aligned} \partial_t T_e = & -\mathbf{v}_E \cdot \nabla T_{e0} - 1.71 \frac{2}{3} T_{e0} \nabla_{\parallel} v_{\parallel e} + \frac{2}{3 N_0} \kappa_{\parallel e} \nabla_{\parallel}^2 T_e \\ & - \frac{2 m_e}{m_i} \nu_e T_e + \mu_T \nabla_{\perp}^2 T_e + S_T + \{\phi, T_e\}. \end{aligned} \quad (4)$$

In these equations, μ_N , μ_T , and μ_{ϕ} are artificial diffusion and viscosity coefficients used for subgrid dissipation. They are large enough to allow saturation and grid convergence²⁶, but small enough to allow for turbulence to develop. In the simulations, they are all given the same value of 1.25×10^{-3} in Bohm-normalized units. This is the only free parameter in the simulations. All other parameters such as the electron collisionality ν_e , ion-neutral collisionality ν_{in} , parallel electron thermal conductivity $\kappa_{\parallel e}$, and mass ratio $\frac{m_i}{m_e}$ are calculated from the experimental parameters. There are two sources of free energy: the density gradient due to the equilibrium density profile N_0 , and the equilibrium electron temperature gradient in T_{e0} , both of which are taken from experimental fits. N_0 and T_{e0} are functions of only the radial cylindrical coordinate r , and they are shown in Fig. 1. The mean potential profile ϕ_0 is set to zero in the model, and terms involving ϕ_0 are not included in Eqns. 1-4. The justification for this is that biasable azimuthal limiters in LAPD allow for the mean $E \times B$ flow and flow shear to be varied with high precision, even allowing the flow to be zeroed out²⁰. The simulations in this paper use the N_0 , T_{e0} , and ϕ_0 profiles from the zeroed out flow experiment, justifying setting the mean potential profile to zero in the simulations.

Simulations also use density and temperature sources (S_n and S_T) in order to keep the

equilibrium profiles from relaxing away from their experimental shapes. These sources suppress the azimuthal averages ($m = 0$ component of the density and temperature fluctuations) at each time step. The azimuthal average of the potential ϕ is allowed to evolve in the simulation, allowing zonal flows to form.

The terms in Poisson brackets are the $E \times B$ advective nonlinearities, which are the only nonlinearities used in the simulations. The numerical simulations are fully spatial in all three dimensions (as opposed to spectral) and use cylindrical annular geometry ($12 < r < 40$ cm). The radial extent used in the simulation encompasses the region where fluctuations are above a few percent in the experiment. Therefore, the radial boundaries are fixed to zero value.

This study analyzes three turbulent simulations which will be referred to as the periodic simulation, the no $n = 0$ simulation, and the sheath simulation. The periodic and no $n = 0$ simulations were also analyzed in a previous paper¹⁷. Both of these simulations enforce periodic boundary conditions in the axial (z) direction. The no $n = 0$ simulation adds an artificial sink-like contribution to Eqns. 1-4 which removes the axial average ($k_{\parallel} = n = 0$ contribution) of the fluctuations at each time step. This no $n = 0$ model essentially eliminates nonlinear instability drive and allows the linear instability to take over the turbulent drive¹⁷. The no $n = 0$ simulation, therefore, serves as a contrast to the periodic simulation in which a nonlinear instability drives the turbulence.

Now the third (sheath) simulation is new. All previous LAPD simulation studies by this group used periodic axial boundary conditions^{17,23-26}. The sheath simulation, as its name implies, uses sheath boundary conditions on the axial machine ends. Specifically, the sheath boundary condition for the parallel current is a linearized Bohm condition:

$$J_{\parallel} = N_0(\phi + \log \sqrt{4\pi m_e/m_i} T_e) \quad (5)$$

where $J_{\parallel} = -N_0 v_{\parallel e}$. The axial boundaries for the other independent fields are implemented with zero derivative (Neumann) boundary conditions, which is consistent with analytical and numerical calculations for such fields in the magnetic pre-sheath region²⁷. This study will in part compare results from the three simulations to help illustrate any effects of the sheath boundary conditions.

As a first comparison, Fig. 2 shows a few statistical characteristics of the density fluctuations for each of the three simulations along with the corresponding characteristics from the

experiment. The periodic simulation clearly has the most similar characteristics to those of the experiment while the no $n = 0$ simulation is most dissimilar. The fluctuations of the sheath simulation have similar statistical properties as those from the experiment, however, the amplitude of the sheath simulation fluctuations is a bit smaller than the experimental fluctuations, especially at small radii.

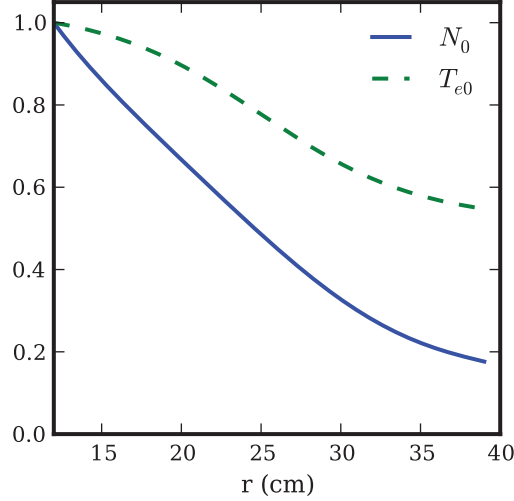


FIG. 1. The profiles of density N_0 and electron temperature T_{e0} used in the simulations normalized to their peak values of $2.86 \times 10^{12} \text{ cm}^{-3}$ and 6 eV, respectively.

III. LINEAR INSTABILITIES

The model described by the equations of Section II contains a few linear instabilities that can all act at the simulated scales. Two of these instabilities are of the electrostatic drift wave type - one is driven by the density gradient and the other by the electron temperature gradient. Both of these instabilities supply energy to the electrostatic potential through parallel compression, called the adiabatic response, and are made unstable by the electron-ion collisional dissipation. These instabilities act under either choice of parallel boundary conditions (periodic or sheath).

The other instability is called the conducting wall mode (CWM) since it is driven by the conducting wall sheaths on the parallel boundaries. Various terms in Eqs. 1-4 can be eliminated to isolate the conducting wall mode. The reduced set of linearized equations are:

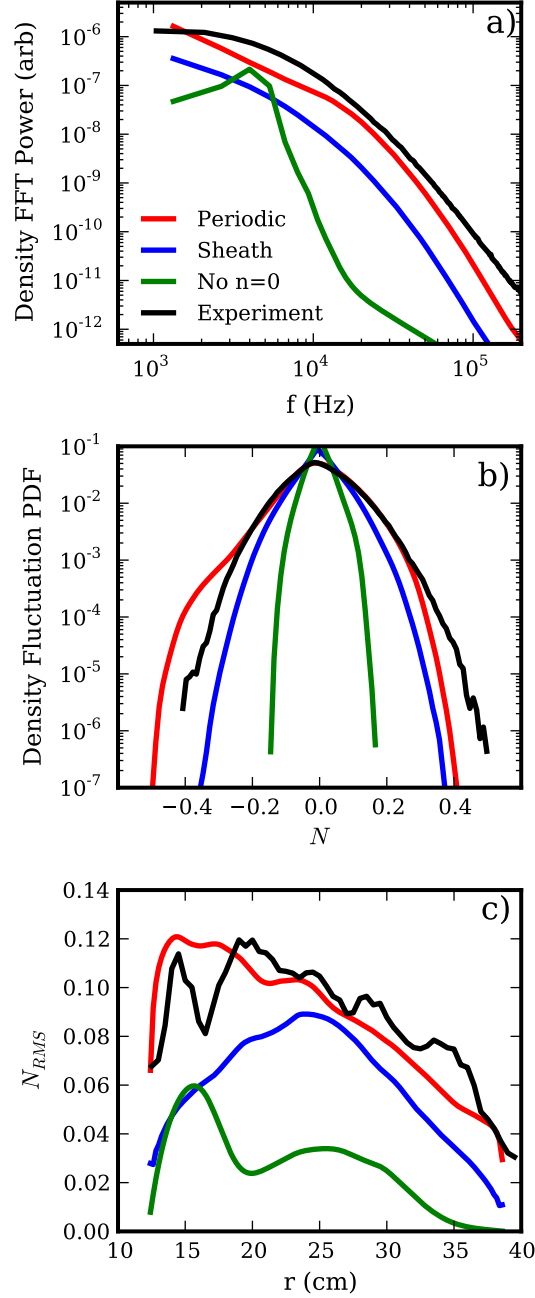


FIG. 2. A comparison of the statistical turbulent properties of the density field. The figures show **a)** the frequency spectrum, **b)** the pdf and **c)** the RMS level of the fluctuations as a function of radius. The various curves use data calculated from the experiment, the simulation with periodic boundary conditions, the simulation with sheath boundary conditions, and a simulation where the $n = 0$ components of the fluctuations are artificially removed.

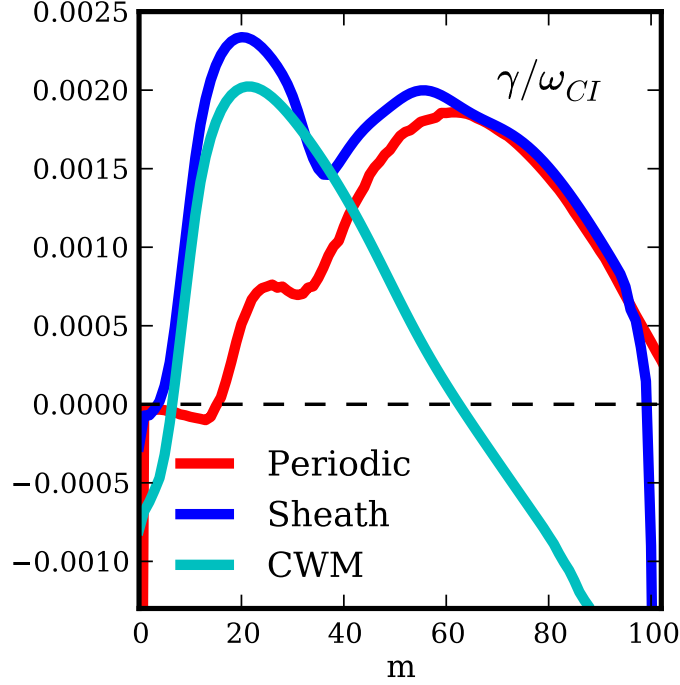


FIG. 3. The growth rates of the drift waves (periodic), the conducting wall mode (CWM), and the full combined model (sheath) as a function of azimuthal wavenumber m .

$$\partial_t v_{\parallel e} = \frac{m_i}{m_e} \nabla_{\parallel} \phi - \nu_e v_{\parallel e}, \quad (6)$$

$$\partial_t \varpi = -N_0 \nabla_{\parallel} v_{\parallel e} - \nu_{in} \varpi + \mu_{\phi} \nabla_{\perp}^2 \varpi, \quad (7)$$

$$\partial_t T_e = -\mathbf{v}_E \cdot \nabla T_{e0} + \frac{2}{3N_0} \kappa_{\parallel e} \nabla_{\parallel}^2 T_e - \frac{2m_e}{m_i} \nu_e T_e + \mu_T \nabla_{\perp}^2 T_e, \quad (8)$$

along with the axial boundary condition given in Eq. 5. The free energy source for this instability is the electron temperature gradient, which is also the free energy for the thermally driven drift waves. However, the adiabatic response is replaced here with a coupling to the potential through the axial boundary condition.

Now, for the experimental parameters and profiles used in the turbulent simulations, the linear growth rates for the drift waves and the conducting wall mode are comparable. The growth rates of the fastest growing linear eigenmode at a given azimuthal wavenumber are shown in Fig. 3. The periodic growth rate curve is found by simulating the linearized versions of Eqs. 1-4 with periodic axial boundary conditions in BOUT++. Therefore, both the density- and temperature-driven drift wave contributions are present for this curve. The

CWM curve is obtained by simulating Eqs. 6-8 with the sheath axial boundary condition of Eq. 5. Finally, the sheath model curve includes the linearized version of Eqs. 1-4 along with the axial sheath boundary condition.

The important result here is that the sheath boundary condition greatly affects the linear stability properties of the system at low azimuthal wavenumber m . The CWM is more unstable than the drift waves for $m < 40$ but less unstable for $m > 40$, and the eigenmode with the highest growth rate has $m = 20$ for the sheath simulation as opposed to $m = 60$ for the periodic simulation. The linear sheath eigenmodes also reflect which of the linear instabilities is active at which wavenumber. In other words, the sheath eigenmodes have CWM character at $m < 40$ and drift wave character at $m > 40$. This manifests itself as differences in axial and radial structure as well as in phase relations between the different scalar fields. However, the linear differences are only significant in the end if they affect the turbulence dynamics. And following a previous paper¹⁷, a great way to study the turbulence dynamics is with an energy dynamics analysis of the turbulent simulations.

IV. ENERGY MACHINERY

In order to perform an energy dynamics analysis on the simulations, expressions for the energy and energy evolution must be derived from Eqs. 1-4. To start, an expression for the normalized energy of the wave fluctuations in the model is defined as:

$$E = \frac{1}{2} \int_V \left[P_0 \left((N/N_0)^2 + \frac{3}{2} (T_e/T_{e0})^2 \right) + N_0 \left(\frac{m_e}{m_i} v_{\parallel e}^2 + (\nabla_{\perp} \phi)^2 \right) \right] dV, \quad (9)$$

where $P_0 = N_0 T_{e0}$ is the equilibrium pressure. The N^2 contribution is the potential energy due to density fluctuations, T_e^2 is the electron temperature fluctuation potential energy, $v_{\parallel e}^2$ is the parallel electron kinetic energy, and $(\nabla_{\perp} \phi)^2$ is the $E \times B$ perpendicular kinetic energy. This energy expression is the physical fluctuation energy. This expression differs slightly from the energy-like expression used in the previous work¹⁷ in that it contains extra factors of N_0 and T_{e0} . The energy-like expression that was analyzed in the previous work was chosen because it had the convenient property that it conserved the advective nonlinearities. The advective nonlinearities are not conserved under the physical energy as defined in Eq. 9, but the advective nonlinearities are also not conserved when the boundaries are not periodic or fixed valued. Since the sheath boundary conditions used in the sheath simulation here do not

ensure that the fields have equal values at each axial boundary, the advective nonlinearities would not be conserved under any general energy expression in any case. So there is no similar advantage in this case to using a special energy-like expression. It is actually more convenient to use the physical energy rather than the special form used in the previous work for a different reason. The reason is that the physical energy conserves the parallel compression dynamics, which means that net energy cannot enter directly into the parallel kinetic energy channel but must make its way via the density or temperature potential energy, which is physically meaningful and simpler to analyze. Now, while the energy-like expression used in the previous work did not preserve this property, the energy that directly entered the parallel kinetic energy channel was too small to matter qualitatively¹⁷.

A more detailed look at the energetic processes comes from a spectral energy analysis. To do this, each fluid field $(N, T_e, v_{\parallel e}, \phi)$ at a given time is Fourier decomposed as $F(r, \theta, z) = \sum_{\vec{k}} f_{\vec{k}}(r) e^{i(m\theta + k_z z)}$, where the subscript \vec{k} represents the spectral wavenumbers, (m, n) , and both positive and negative wavenumbers are included in the sums. m is the azimuthal wavenumber while n is the axial integer wavenumber such that $k_{\parallel} \equiv k_z = 2\pi n/l_z$. Note that the radial direction is not spectrally decomposed because it is too complicated with a global simulation. With this, the energy of each Fourier $\vec{k} = (m, n)$ mode is

$$E_{tot}(\vec{k}) = \frac{1}{2} \left\langle \frac{T_{e0}}{N_0} |n_{\vec{k}}|^2 + \frac{3N_0}{2T_{e0}} |t_{\vec{k}}|^2 + \frac{m_e}{m_i} N_0 |v_{\vec{k}}|^2 + N_0 \left| \frac{\partial \phi_{\vec{k}}}{\partial r} \right|^2 + N_0 \frac{m^2}{r^2} |\phi_{\vec{k}}|^2 \right\rangle, \quad (10)$$

where the brackets $\langle \rangle$ represent the radial integral: $\int_{r_a}^{r_b} r dr$. The energy evolution for each Fourier mode of each field has the form:

$$\frac{\partial E_j(\vec{k})}{\partial t} = Q_j(\vec{k}) + C_j(\vec{k}) + D_j(\vec{k}) + \sum_{\vec{k}'} T_j(\vec{k}, \vec{k}'). \quad (11)$$

The index j stands for each field, (n, t, v, ϕ) , and the sum over j gives the total energy evolution. Note that with the conventions used, the symbol n denotes both the axial mode number as well as the Fourier coefficient of the density fluctuation. The differences should be clear in context. The derivation of Eq. 11 is given in the previous work¹⁷. $T_j(\vec{k}, \vec{k}')$ is the nonlinear energy transfer function that comes from the advective nonlinearities. It describes the nonlinear energy transfer rate of fluctuations with $\vec{k}' = (m', n')$ to fluctuations with $\vec{k} = (m, n)$. For example, a positive value of $T_t(\vec{k}, \vec{k}')$ indicates that temperature

fluctuations at wavenumber \vec{k} gain energy from temperature fluctuations at wavenumber \vec{k}' , with the process mediated by flow fluctuations at wavenumber $\vec{k} - \vec{k}'$.

The linear terms are broken up into three contributions in Eq. 11. $D_j(\vec{k})$ represents energy dissipation due to collisions, artificial diffusion and viscosity, and the density and temperature sources. Each contribution to $D_j(\vec{k})$ is negative. $C_j(\vec{k})$ contains the linear terms dubbed “transfer channels”¹⁴. They are rewritten here:

$$C_n(\vec{k}) = Re \left\{ \left\langle -ik_z T_{e0} v_{\vec{k}} n_{\vec{k}}^* \right\rangle \right\} \quad (12)$$

$$C_v(\vec{k}) = Re \left\{ \left\langle -ik_z T_{e0} n_{\vec{k}} v_{\vec{k}}^* + ik_z N_0 \phi_{\vec{k}} v_{\vec{k}}^* - 1.71 ik_z N_0 t_{\vec{k}} v_{\vec{k}}^* \right\rangle \right\} \quad (13)$$

$$C_\phi(\vec{k}) = Re \left\{ \left\langle ik_z N_0 v_{\vec{k}} \phi_{\vec{k}}^* \right\rangle \right\} \quad (14)$$

$$C_t(\vec{k}) = Re \left\{ \left\langle -1.71 ik_z N_0 v_{\vec{k}} t_{\vec{k}}^* \right\rangle \right\} \quad (15)$$

First, note that the real part operators are written explicitly in these expressions since the imaginary part of these expressions would cancel with the imaginary part of the corresponding terms with $-\vec{k}$. Second, notice that $C_n(\vec{k}) + C_v(\vec{k}) + C_\phi(\vec{k}) + C_t(\vec{k}) = 0$. This is the reason why these terms are called transfer channels. They represent the transfer between the different types of energy of the different fields ($N, \phi, T_e \leftrightarrow v_{\parallel e}$), but taken together, they do not create or dissipate total energy from the system. The only energy transfer between different fields in this system is through the parallel electron velocity (parallel current) dynamics. There is no direct transfer between the state variables N, ϕ , and T_e . Altogether, the coupling through the parallel current is called the adiabatic response. It is an essential part of both the linear and nonlinear drift wave mechanisms^{14,16}. The adiabatic response moves energy from the pressure fluctuations to the perpendicular flow through the parallel current.

Finally, the $Q_j(\vec{k})$ terms represent the nonconservative energy sources. They are rewritten here:

$$Q_n(\vec{k}) = Re \left\{ \left\langle -\frac{imT_{e0}}{N_0 r} \partial_r N_0 \phi_{\vec{k}} n_{\vec{k}}^* \right\rangle \right\} \quad (16)$$

$$Q_v(\vec{k}) = 0 \quad (17)$$

$$Q_\phi(\vec{k}) = 0 \quad (18)$$

$$Q_t(\vec{k}) = Re \left\{ \left\langle -\frac{3}{2} \frac{imN_0}{T_{e0} r} \partial_r T_{e0} \phi_{\vec{k}} t_{\vec{k}}^* \right\rangle \right\} \quad (19)$$

$Q_n(\vec{k})$ is the energy extraction from the equilibrium density profile into the density fluctuations. This term may have either sign depending on the phase relation between $\phi_{\vec{k}}$ and $n_{\vec{k}}$, so it can in fact dissipate fluctuation potential energy from the system as well as create it at each \vec{k} . $Q_t(\vec{k})$ is completely analogous to $Q_n(\vec{k})$ but for the temperature rather than the density. $Q_v(\vec{k})$ and $Q_\phi(\vec{k})$ are zero because the parallel and perpendicular flow fluctuations obtain energy only through the adiabatic response, not directly through the free energy in the equilibrium gradients.

V. ENERGY DYNAMICS RESULTS

The diagrams in Fig. 4 summarize the flow of energy for the periodic and sheath simulations. Each of the functions, such as $Q_n(m, n)$, is a function of m and n , making visualization of all of these functions difficult. So the terms in the diagrams are summed over m . Additionally, all of the $n \neq 0$ terms are summed over as well. The $n = 0$ contribution is separated from the other n components because the $n = 0 \leftrightarrow n \neq 0$ dynamic is the primary factor that determines whether the linear instability or the nonlinear instability dominates the energy drive¹⁷.

In these diagrams, the source of energy into the fluctuations is free energy in the equilibrium gradients, ∇N_0 and ∇T_{e0} . The arrows labeled Q_n and Q_t represent energy injection from the equilibrium gradients into the fluctuations, $n(\vec{k})$ and $t(\vec{k})$. The four Q arrows contain values that sum to 100 (by choice of normalization). Since the Q pathways are the only pathways that deposit net energy into the fluctuations, the numbers in all arrows represent a percentage of the total energy injected into the system. Now, a majority of the energy deposited into the fluctuations (71% for the periodic simulation and 56% for the sheath simulation) is from the density gradient into the $n = 0$ density fluctuations. This is not a path allowed by any of the linear instabilities in the system since the linear instabilities can only deposit energy into $n \neq 0$ fluctuations. In fact, in this turbulent state, more energy is transferred by nonlinear three-wave coupling into $n \neq 0$ fluctuations than by direct injection from the equilibrium gradients. The three-wave coupling is represented by the T_n and T_t arrows. The direction of these arrows is from $n = 0 \rightarrow n \neq 0$, which is opposite to that expected from the common cascading type turbulent paradigm where the linear instability dominates the turbulent injection dynamics and three-wave processes transfer energy to

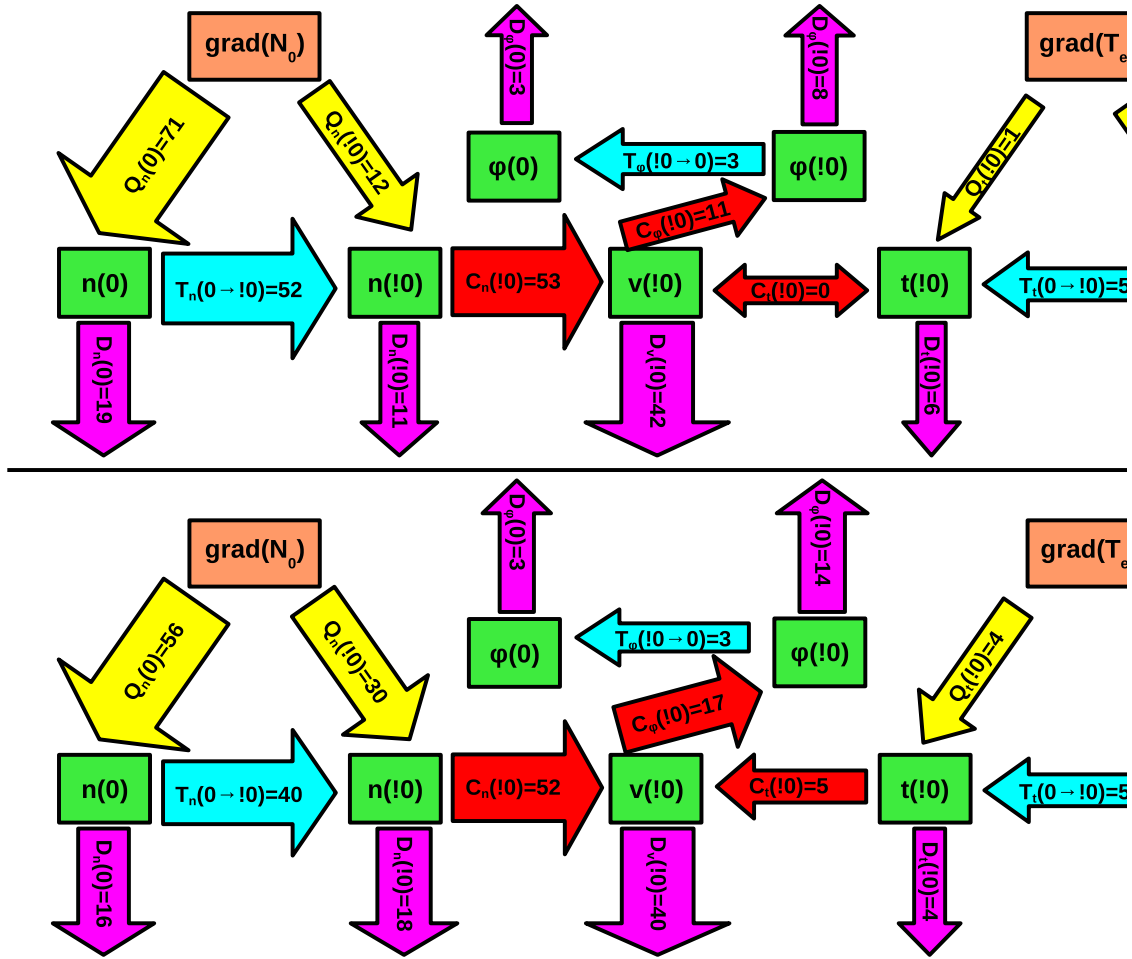


FIG. 4. Summary of the energy dynamics for the **a)** periodic case and **b)** sheath boundary case. Each arrow contains the sum over all m . The 0's in the parentheses represent the $n = 0$ modes while the !0's represent a sum over the n modes for $n \neq 0$. The values in the arrows represent the percentage of total energy that goes through the channel represented by the arrow. The size of the arrows gives a rougher but more visual indication of the amount of energy going through each channel.

waves that are linearly stable.

The reason why all of the non-dissipated energy that is injected into $n = 0$ density and temperature structures goes into $n \neq 0$ density and temperature potential energy structures rather than into $n = 0$ kinetic energy structures is that potential to kinetic energy transfer can only work through the adiabatic response, which requires $n \neq 0$. Actually, in the sheath simulation, potential energy can transfer to kinetic energy through the axial boundaries, but this still requires $n \neq 0$ and it works only through the temperature fluctuations, which are less important than the density fluctuations in the simulations. Note, in fact, that this sheath boundary transfer channel isn't included in the energy dynamics calculations. So the main transfer channel from potential to kinetic energy, shown by the C_n , C_t , and C_ϕ arrows, is the adiabatic response. The adiabatic response takes energy from the $n \neq 0$ density and temperature fluctuations and transfers it into the parallel velocity fluctuations (C_n and C_t , respectively). It then transfers some of this energy into $n \neq 0$ potential fluctuations (C_ϕ), while much of the fluctuation energy is ohmically dissipated (D_v).

The final step of the energy dynamics process is a three-wave axial wavenumber transfer from potential fluctuations at $n \neq 0$ to potential fluctuations at $n = 0$, which are of course necessary in making the $Q_n(0)$ and $Q_t(0)$ terms finite. Meanwhile, dissipation acts on all fluctuations, which is quantified by the D arrows throughout. A couple of interesting features are evident from the diagrams in Fig. 4. First, the turbulent dynamics in both simulations are dominated by the nonlinear instability process described above and in Friedman et al.¹⁷ rather than the paradigmatic process of linear instability energy injection followed by nonlinear cascading. And second, the periodic and sheath simulations have qualitatively similar dynamics despite the fact that the linear stability properties of the two cases are qualitatively different. This speaks to the robustness of the nonlinear instability.

A more compact way to see the similarity of the instability process in the periodic and sheath simulations is shown in Fig. 5. This figure shows the turbulent growth rate of the two simulations along with that of the no $n = 0$ simulation, which really contrasts the periodic and sheath simulations. The turbulent growth rate is defined as the net energy injection into the fluctuations minus the dissipation out of them, all divided by the total energy. The conservative transfers are of course not part of the growth rates. Formally, $\gamma(\vec{k}) = (\sum_j Q_j(\vec{k}) + D_j(\vec{k}))/E_{tot}(\vec{k})$, where the index j represents the different fields. Since the growth rates sum over the fields, it's not as difficult to view them in their full wavenumber

space (both in m and n). However, almost all of the energy in the simulations is contained in $n = 0$ and $n = 1$ fluctuations, so $n > 1$ fluctuations are not shown in the figure. It should be noted, however, that Fourier decomposing the sheath simulation in the axial direction is less ideal than doing so in the periodic simulation. Fourier modes are not as natural a basis in the sheath simulation, and the $n = 1$ Fourier mode does not perfectly represent the linear eigenmode structure as it does for the periodic and no $n = 0$ simulations. A more detailed discussion of this point is left to the Appendix, but in summary, the $n = 1$ Fourier mode does capture enough of the sheath linear eigenmode structure to make the Fourier decomposition useful for this simulation.

Figure 5 illustrates the true dominance of the nonlinear instability in the positive $n = 0$ energy growth rate and negative $n = 1$ growth rate for the periodic and sheath simulations. The signs of these growth rates are the opposite of those for the linear instability. The figure also reveals the remarkable similarity in the nonlinear energy dynamics processes between the periodic and sheath simulations. This is in stark contrast to the no $n = 0$ simulation, which has an $n = 1$ growth rate similar to the linear growth rate (Fig. 3) and a negative $n = 0$ growth rate. Note that even though the $n = 0$ fluctuation components are removed from the no $n = 0$ simulation at each time step, $n = 0$ fluctuations are nonlinearly excited (by three-wave transfer) by the $n \neq 0$ fluctuations, and therefore, they do have small but finite amplitude prior to their removal, which can be used to calculate the growth rate of these modes. Furthermore, the turbulent growth rate of the $n = 1$ component of the no $n = 0$ simulation is slightly less than the linear growth rate for all m due to the fact that eigenmodes other than the fastest growing ones are nonlinearly excited in the turbulent simulation, thus damping the growth rate. This no $n = 0$ growth rate picture is just that of the turbulence paradigm of linear instability with cascading dynamics.

VI. LINEAR VS NONLINEAR STRUCTURE CORRELATION

A. Energy in the Fastest Growing Eigenmodes

Now it may be the case that in simulations dominated by a linear instability, the fastest growing linear eigenmode dominates the system, nonlinearly transferring some energy to more weakly unstable or even stable eigenmodes. In this case, a large portion of the energy may

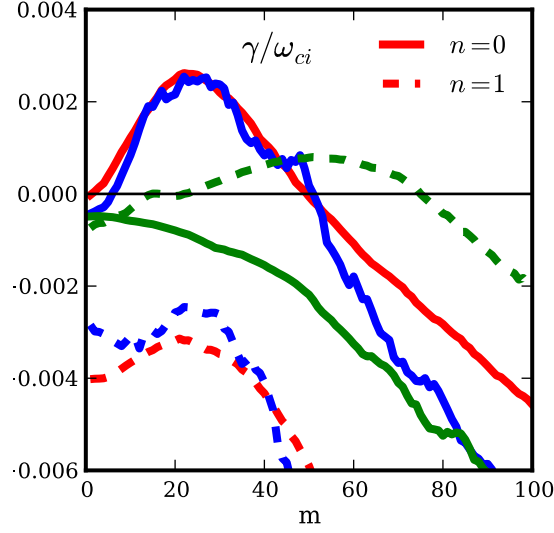


FIG. 5. The turbulent growth rates defined as $\gamma = \frac{\partial E_{tot}}{\partial t} / (2E_{tot})$ where only the linear terms are included in $\frac{\partial E_{tot}}{\partial t}$. The $n = 0$ (solid) and $n = 1$ (dashed) growth rates are displayed as a function of m .

remain in the fastest growing linear eigenmode²⁸. In the case where a nonlinear instability is dominant, the linear eigenmode should have little bearing on the structure of the turbulence and therefore little energy should be contained in this eigenmode. Therefore, a gauge of whether a linear or nonlinear instability dominates a system is the fraction of energy in a turbulent system that is contained in the fastest growing linear eigenmode. This may be calculated by projecting the fastest growing eigenmode onto the turbulent state.

Formally, in the model considered in this study, the turbulent state is fully described by four independent fields, which can be appended into a single vector of the spatio-temporal field functions: $f_{turb}(\vec{r}, t) = \{N(\vec{r}, t), T_e(\vec{r}, t), \nabla_{\perp} \phi(\vec{r}, t), v_{\parallel e}(\vec{r}, t)\}$. This vector may be decomposed in a complete basis:

$$f_{turb}(\vec{r}, t) = \sum_{i,m} c_{i,m}(t) v_{i,m}(r, z) e^{im\theta}, \quad (20)$$

where $v_{i,m}(r, z)$ are time-independent spatial complex basis functions of the form $v_{i,m}(r, z) = \{n_{i,m}(r, z), t_{i,m}(r, z), \nabla_{\perp} \phi_{i,m}(r, z), v_{i,m}(r, z)\}$, and $c_{i,m}(t)$ are the complex time-dependent amplitudes. The θ dependence of the basis functions has been explicitly imposed as a Fourier basis. The total number of linearly independent basis functions is the number of

total grid points used in the simulation times the number of independent fields, which is four in this case. Now, $v_{i,m}(r, z)$ can be any linearly independent set of functions and need not be the linear eigenfunctions of the system. In fact, the linear eigenfunctions of the equations used here are not orthogonal, and are thus not very useful to consider. However, it is quite useful to set $v_{0,m}(r, z)$ to the fastest growing linear eigenmode because this is the structure of interest that is to be projected onto the turbulence. The other $v_{i \neq 0,m}(r, z)$ comprise the remainder of the orthonormal basis, and they must be different from the remaining linear eigenfunctions in order to complete the orthogonal basis. It isn't necessary for the purpose of this study to actually compute these other basis functions, but if one were to compute them, one might start with all of the linear eigenmodes and perform a Gram-Schmidt orthogonalization procedure, making sure to start with the fastest growing eigenmode in order to preserve it. Using this procedure, Hatch et al.²⁸ found that a significant fraction ($\sim 50\%$) of the energy in a turbulent state of ITG turbulence was contained in the fastest growing linear eigenmode at each perpendicular wavenumber. Such a result, however, doesn't require knowledge of the other basis functions, and thus they are not computed here.

Now, to compute this fraction, first define an inner product that is energetically meaningful and that sets the orthonormality of the basis functions:

$$\langle v_{i,m}, v_{j,m} \rangle = \int w v_{i,m}^* \cdot v_{j,m} dV = \delta_{i,j}. \quad (21)$$

The weighting w is such that $\langle f_{turb}, f_{turb} \rangle = E_{turb}$. Now from Eqs. 20 and 21, $\langle f_{turb}, f_{turb} \rangle = E_{turb} = \sum_{i,m} |c_{i,m}|^2$ and $\langle f_{turb,m}, f_{turb,m} \rangle = E_{turb,m} = \sum_i |c_{i,m}|^2$. Then, the amount of energy contained in the fastest growing mode (for each m) is given by the square of the projection of the mode onto the turbulence: $E_{0,m} = |\langle v_{0,m}, f_{turb,m} \rangle|^2 = |c_{0,m}|^2$. The ratio $R_m = E_{0,m}/E_{turb,m}$ is a measure of the fraction of turbulent energy contained in the fastest growing linear eigenmode.

Of course, $E_{turb,m}$ is easily calculated from the turbulent state, but $E_{0,m}$ in the turbulent state can only be found with knowledge of the fastest growing eigenfunction. The fastest growing eigenfunction, though, can be found easily by running a simulation from a random or turbulent state with all of the nonlinearities removed from the model equations as was done in Section III. After some time, the fastest growing eigenfunctions will come to dominate the fluctuation structure. Then, a Fourier decomposition in m space will separate the fastest growing eigenfunctions at each m , including the real and imaginary part of the

eigenfunctions (up to a time dependent complex constant, which is removed by normalizing the eigenfunction). These eigenfunctions can then be projected onto the turbulent state with the inner product defined in Eq. 21, giving $E_{0,m}$.

The ratio R_m is shown in Fig. 6 for the three simulations. As expected, the periodic simulation has a small value of the ratio ($R_m < 0.07$) for all m . This confirms that the turbulence largely self-organizes without regard to the linear physics. In fact, R_m rapidly declines for $m < 40$, going all the way down to about 10^{-5} . This region is where the nonlinear instability is strongest and where $n = 0$ structures dominate the energy spectrum¹⁷. It is not surprising then that the fastest growing linear eigenfunctions, which have $n = 1$, don't make up much of the energy of the signal. Also not surprising is that the fastest growing eigenfunctions make up a significant fraction of the energy in the no $n = 0$ simulation. Where the linear drift wave instability is the strongest (at $m \sim 60$), $R_m \sim 0.5$. Clearly, the linear physics dominates the no $n = 0$ simulation.

The sheath simulation ratio result TBD since the wrong linear modes are being used currently.

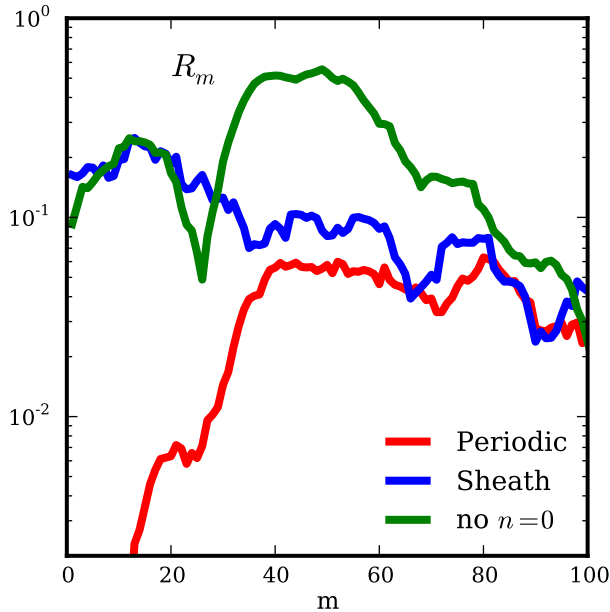


FIG. 6. R_m for all m for the periodic, sheath, and no $n = 0$ simulations.

B. Quasilinear Flux

Another consequence of the linear instability being overshadowed by the nonlinear instability in the turbulent state is that calculations of turbulent characteristics that rely upon linear properties may be inaccurate or misleading. An obvious contender for such a calculation is the quasilinear flux. The electrostatic radial particle flux through a given flux surface is

$$\Gamma(r) = \int n v_r dS = - \int \sum_m i m n_m \phi_m^* dz. \quad (22)$$

The flux in the turbulent state depends upon the correlation of two independent quantities, however, a widely used method for evaluating the correlation between the density and potential is to use a linear eigenvector to express $n(m)$ in terms of the potential: $n(m) = L(m)\phi(m)$, where $L(m)$ is the linear response function²⁹. Alternatively, the potential may be written in terms of the density: $\phi(m) = L^{-1}(m)n(m)$. The response function may be calculated analytically or using results from a linear simulation. An analytic calculation is used here because that is more common. Substitution of these linear relationships into Eq. 22 yields expressions for the quasilinear flux:

$$\Gamma_{\phi,QL}(r, m) = \int -im|\phi(m)|^2 L(m) dz \quad (23)$$

$$\Gamma_{n,QL}(r, m) = \int -im|n(m)|^2 L^{-1*}(m) dz. \quad (24)$$

Which of these two expressions is used depends upon the quantity that one measures, density or potential. The amplitudes $|\phi(m)|^2$ and $|n(m)|^2$ are obtained from the turbulent state, but the linear response function must be obtained from the linear eigenvectors, typically the fastest growing linear eigenvectors. Clearly, if the turbulence is largely composed of the linear eigenvectors, the two form of Γ_{QL} in Eqs. 23 and 24 would produce similar results. However, even in the no $n = 0$ simulation in which the turbulent dynamics is dominated by a linear instability, less than 50% of the turbulent energy is contained in the fastest growing eigenfunctions.

The full nonlinear flux and the quasilinear fluxes are shown for the three simulations in Fig. 7 as both a function of m (summed over radius) and a function of r (summed over m).

Surprisingly, the quasilinear flux amplitudes match the nonlinear flux amplitudes quite well for the periodic and sheath simulations but not for the no $n = 0$ simulation. However, the fact that the quasilinear flux overpredicts the flux for the no $n = 0$ simulation is expected because the non-fastest growing eigenmodes that account for over 50% of the turbulent energy cause less flux than the fastest growing eigenmode²⁹. The same reasoning was used above in discussing why the turbulent growth rate for the $n = 1$ mode in this simulation is less than the linear $n = 1$ growth rate, seen in Fig. 5. The expression for the flux is, after all, essentially the same as the expression for the nonconservative energy source (see Eq. 16), which is the most important part of the growth rate.

Now for the periodic simulation, even though the nonlinear and quasilinear flux amplitudes are similar, the radial shapes of the quasilinear fluxes differ from each other and from the nonlinear flux. This is indicative of the fact that the linear eigenfunctions are poorly representative of the turbulent state, especially at low m . The sheath simulation has a better spatial match, which is expected due to the greater linear character of the turbulence in this simulation, however, the rather high degree of similarity is somewhat surprising.

VII. CONCLUSION

The observation of filamentary $k_{\parallel} = 0$ structures is prevalent in many different kinds of experiments and simulations, yet their presence is most often attributed to linear instabilities such as flow-driven Kelvin-Helmholtz or interchange instabilities. Very rarely are nonlinear instabilities considered. In simulations at least, there is no excuse in using indirect evidence to classify a type of turbulence because the spatial information allows one to perform energetics analyses. Experiments don't have such a luxury, but this should be motivation to try to numerically simulate experiments.

Through simulation of a particular LAPD experiment, this paper has shown a nonlinear instability to be the driving force behind the turbulence. More accurately, this paper has extended earlier work¹⁷ that showed this. However, this extension is important because it deals with the matter of axial boundary conditions, and the nonlinear instability depends on axial wave dynamics, so the boundary conditions could have greatly affected this. And although the axial sheath boundary conditions used here do have a significant qualitative effect on the linear instabilities of the system, they do not affect the turbulence in a significant way.

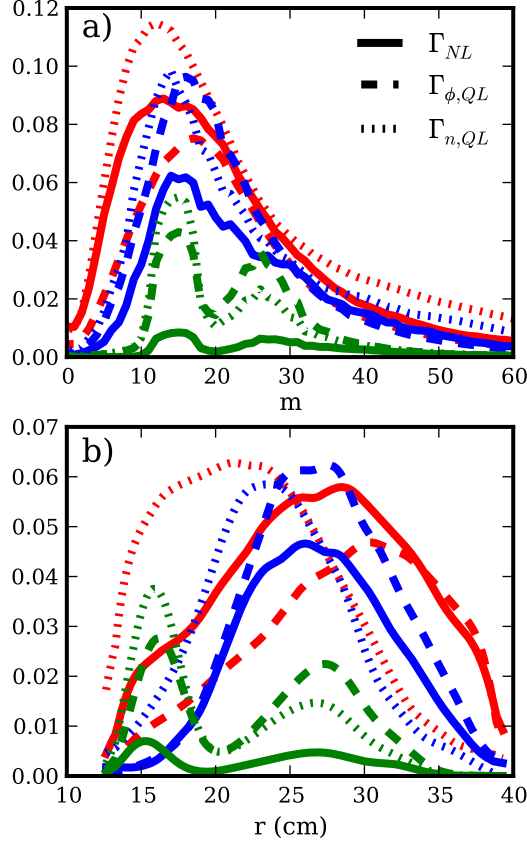


FIG. 7. The radial particle flux calculated from the turbulence (γ_{NL}) vs. the corresponding quasilinear flux using equations 23 and 24. **a)** Shows the flux as a function of m and **b)** shows the flux as a function of r . For reference to the curves in **b)**, the Bohm flux is about 0.1, which is just about a factor of two higher than the flux for the periodic and sheath simulations, but an order of magnitude higher than the no $n = 0$ simulation flux.

Specifically, the nonlinear instability that preferentially drives $k_{\parallel} = 0$ structures remains robust to the change in boundary conditions. Quantitatively, the sheath boundary conditions do cause the linear instability to be more competitive with the nonlinear instability, but not to the point of taking over. This should be expected from the prediction by Scott¹⁶ that the linear drift waves should dominate when their linear growth rate is larger than their frequency. This isn't the case for either the periodic or sheath simulations, however, it is closer to being true for the sheath simulation.

ACKNOWLEDGMENTS

This research was performed under appointment to the Fusion Energy Sciences Fellowship Program administered by Oak Ridge Institute for Science and Education under a contract between the U.S. Department of Energy and the Oak Ridge Associated Universities.

Appendix A: Non-periodic Fourier Decomposition

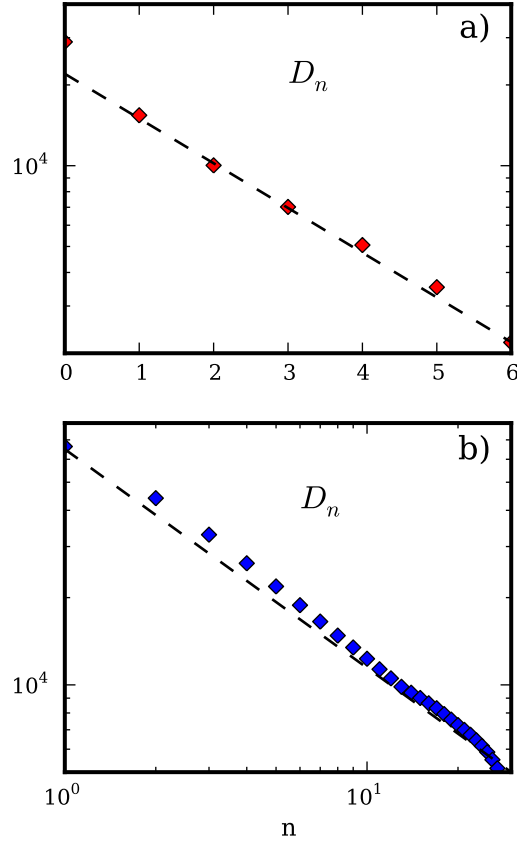


FIG. 8. D_n for **a)** The simulation with periodic axial boundaries displaying exponential convergence and **b)** the simulation with sheath axial boundaries displaying algebraic convergence.

It is well known that Fourier reconstructions of signals that contain discontinuities or non-periodic boundaries are subject to Gibbs phenomena. A clear indication of this is the convergence properties of the Fourier reconstructions. Take a discrete signal with the

following Fourier decomposition:

$$f(x) = \sum_{k=-N}^N \hat{f}_k e^{2\pi i k x}, \quad (\text{A1})$$

where the \hat{f}_k are ordered in the sum by the size of their absolute value with \hat{f}_0 being the largest Fourier coefficient. The Fourier reconstruction of order $n < N$ is then:

$$g_n(x) = \sum_{k=-n}^n \hat{f}_k e^{2\pi i k x} \quad (\text{A2})$$

There are several types of convergences of the g_n , one of which is the $L1$ norm. Defining the difference between the original signal and the Fourier reconstruction of order n as $D_n = \sum_x |f(x) - g_n(x)|$, one can look at the convergence of D_n as a function of n . For periodic signals, D_n converges exponentially, while it only converges algebraically (power law) for non-periodic or discontinuous signals.

D_n is plotted for the cases of the periodic and sheath simulations in Fig. 8. Even though the x-axis label n indicates the mode with the n^{th} largest amplitude by construction of Eq. A2, it also happens to correspond to the axial mode number for all but the last few n . In other words, in both simulations, most of the energy is contained in $n = 0$ modes followed by $n = 1$ modes and so on. Therefore, in reality, the axial Fourier decomposition is a useful tool for even the sheath simulation despite the fact that Fourier modes are not natural eigenmodes in this case.

REFERENCES

- ¹R. E. Waltz. Subcritical magnetohydrodynamic turbulence. *Phys. Rev. Lett.*, 55:1098, 1985.
- ²B. D. Scott. Self-sustained collisional drift-wave turbulence in a sheared magnetic field. *Phys. Rev. Lett.*, 65:3289, 1990.
- ³B. D. Scott. The mechanism of self sustainment in collisional drift wave turbulence. *Phys. Fluids B*, 4:2468, 1992.
- ⁴H. Nordman, V. P. Pavlenko, and J. Weiland. Subcritical reactive drift wave turbulence. *Phys. Fluids B*, 5:402, 1993.

- ⁵K. Itoh, S. I. Itoh, M. Yagi, and A. Fukuyama. Subcritical excitation of plasma turbulence. *Journal of the Physical Society of Japan*, 65:2749–2752, 1996.
- ⁶E. G. Highcock, A. A. Schekochihin, S. C. Cowley, M. Barnes, F. I. Parra, C. M. Roach, and W. Dorland. Zero-turbulence manifold in a toroidal plasma. *Phys. Rev. Lett.*, submitted.
- ⁷A. M. Dimits, G. Bateman, and et al. Comparisons and physics basis of tokamak transport models and turbulece simulations. *Phys. Plasmas*, 7:969, 2000.
- ⁸D. R. Ernst, P. T. Bonoli, and et al. Role of trapped electron mode turbulence in internal transport barrier control in the alcator c-mod tokamak. *Phys. Plasmas*, 11:2637, 2004.
- ⁹D. Biskamp and A. Zeiler. Nonlinear instability mechanism in 3d collisional drift-wave turbulence. *Phys. Rev. Lett.*, 74:706, 1995.
- ¹⁰J. F. Drake, A. Zeiler, and D. Biskamp. Nonlinear self-sustained drift-wave turbulence. *Phys. Rev. Lett.*, 75:4222, 1995.
- ¹¹A. Zeiler, D. Biskamp, J. F. Drake, and P. N. Guzdar. Three-dimensional fluid simulations of tokamak edge turbulence. *Phys. Plasmas*, 3:2951, 1996.
- ¹²A. Zeiler, J. F. Drake, and D. Biskamp. Electron temperature fluctuations in drift-resistive ballooning turbulence. *Phys. Plasmas*, 4:991, 1997.
- ¹³S. B. Korsholm, P. K. Michelsen, and V. Naulin. Resistive drift wave turbulence in a three-dimensional geometry. *Phys. Plasmas*, 6:2401, 1999.
- ¹⁴B. D. Scott. The nonlinear drift wave instability and its role in tokamak edge turbulence. *New J. Physics*, 4:52.1–52.30, 2002.
- ¹⁵B. D. Scott. Computation of electromagnetic turbulence and anomalous transport mechanisms in tokamak plasmas. *Plasma Phys. Control. Fusion*, 45:A385–A398, 2003.
- ¹⁶B. D. Scott. Drift wave versus interchange turbulence in tokamak geometry: Linear versus nonlinear mode structure. *Phys. Plasmas*, 12:062314, 2005.
- ¹⁷B. Friedman, T. A. Carter, M. V. Umansky, D. Schaffner, and B. Dudson. Energy dynamics in a simulation of lapd turbulence. *Phys. Plasmas*, 19:102307, 2012.
- ¹⁸W. Gekelman, H. Pfister, Z. Lucky, J. Bamber, D. Leneman, and J. Maggs. Design, construction and properties of the large plasma research device - the lapd at ucla. *Rev. Sci. Inst.*, 62:2875, 1991.
- ¹⁹H. L. Berk, D. D. Ryutov, and Yu. A. Tsidulko. Temperature-gradient instability induced by conducting end walls. *Phys. Fluids B*, 3:1346, 1991.
- ²⁰D. A. Schaffner, T. A. Carter, G. D. Rossi, D. S. Guice, J. E. Maggs, S. Vincena, and

- B. Friedman. Modification of turbulent transport with continuous variation of flow shear in the large plasma device. *Phys. Rev. Lett.*, 109:135002, 2012.
- ²¹S I Braginskii. Transport processes in a plasma. In M A Leontovich, editor, *Reviews of Plasma Physics*, volume 1, pages 205–311. Consultants Bureau, New York, 1965.
- ²²B. D. Dudson, M. V. Umansky, X. Q. Xu, P. B. Snyder, and H. R. Wilson. Bout++: A framework for parallel plasma fluid simulations. *Computer Physics Communications*, pages 1467–1480, 2009.
- ²³P. Popovich, M. V. Umansky, T. A. Carter, and B. Friedman. Analysis of plasma instabilities and verification of bout code for linear plasma device. *Phys. Plasmas*, 17:102107, 2010.
- ²⁴P. Popovich, M. V. Umansky, T. A. Carter, and B. Friedman. Modeling of plasma turbulence and transport in the large plasma device. *Phys. Plasmas*, 17:122312, 2010.
- ²⁵M. V. Umansky, P. Popovich, T. A. Carter, B. Friedman, and W. M. Nevins. Numerical simulation and analysis of plasma turbulence the large plasma device. *Phys. Plasmas*, 18:055709, 2011.
- ²⁶B. Friedman, M. V. Umansky, and T. A. Carter. Grid convergence study in a simulation of lapd turbulence. *Contrib. Plasma Phys.*, 52:412–416, 2012.
- ²⁷J. Loizu, P. Ricci, F. Halpern, and S. Jolliet. Boundary conditions for plasma fluid models at the magnetic presheath entrance. *Phys. Plasmas*, submitted.
- ²⁸D. R. Hatch, P. W. Terry, F. Jenko, F. Merz, and W. M. Nevins. Saturation of gyrokinetic turbulence through damped eigenmodes. *Phys. Rev. Lett.*, 106:115003, 2011.
- ²⁹P. W. Terry and R. Gatto. Nonlinear inward particle flux component in trapped electron mode turbulence. *Phys. Plasmas*, 13:062309, 2006.